Journal of Environmental Chemical Engineering 10 (2022) 107655

Contents lists available at ScienceDirect

Journal of Environmental Chemical Engineering

journal homepage: www.elsevier.com/locate/jece

Noble metal modified (002)-oriented ZnO hollow spheres for the degradation of a broad range of pollutants

Zoltán Kovács [a,b,c], Viktória Márta [a,c], Tamás Gyulavári [a,c], Áron Ágoston [d], Lucian Baia [b,e], Zsolt Pap [c,e,*], Klara Hernadi [a,c,f,**]

[a] Research Group of Environmental Chemistry, Institute of Chemistry, University of Szeged, Tisza Lajos krt. 103, H-6720 Szeged, Hungary
[b] Faculty of Physics, Babeș-Bolyai University, Str. Mihail Kogălniceanu. 1, RO-400084 Cluj-Napoca, Romania
[c] Department of Applied and Environmental Chemistry, University of Szeged, Rerrich tér 1, H-6720 Szeged, Hungary
[d] Department of Physical Chemistry and Materials Sciences, University of Szeged, Aradi v.t.1, H-6720 Szeged, Hungary
[e] Centre of Nanostructured Materials and Bio-Nano Interfaces, Institute for Interdisciplinary Research on Bio-Nano-Sciences, Treboniu Laurian street 42, Cluj-Napoca RO-400271, Romania
[f] Institute of Physical Metallurgy, Metal Forming and Nanotechnology, University of Miskolc, Miskolc-Egyetemváros, C/2-5, H-3515 Miskolc, Hungary

ARTICLE INFO

Editor: Teik Thye Lim

Keywords:
Zinc oxide
Hollow spheres
Noble metals
Photocatalysis

ABSTRACT

Zinc oxide hollow spheres were fabricated by applying sucrose-derived carbon spheres as templates that were eliminated through calcination. For this purpose, two synthesis methods were examined and compared, chemical impregnation and solvothermal method. The most suitable ZnO hollow structure was selected for noble metal deposition (Au and Pt at 1 wt%) to further increase the photocatalytic activity. The photocatalytic activity was examined by the decomposition of three different model pollutants (phenol, Na-ibuprofen and diuron) under UV irradiation. The as-synthesized hollow sphere structures and its noble metal composites were further examined by XRD, SEM, IR, DRS, PL. The templates did not modify the structure of ZnO only the morphology and contributed to the preservation of the original structure during calcination. The structural, optical and photocatalytic activity was correlated with both the application of carbon sphere template, and noble metal deposition respective their role in the improvement of the photocatalytic activity.

1. Introduction

Heterogenous photocatalysis has become one of the most flourishing research fields in the last three decades. One of its most promising application possibilities is to use it as an alternative technique for wastewater treatment. The most appealing characteristics of the method are its non-selectivity, versatility and that it qualifies as a green method [1]. Zinc oxide is one of the most researched and promising semiconductors for photocatalytic applications because it is cheap, accessible, non-toxic, and it has high UV absorption and a large variety of synthesis methods [2]. However, there is still room for improvement regarding its photocatalytic efficiency, making this aspect the main scope of numerous publications. A few of the most common approaches are the following: using different synthesis methods (sol-gel [3], hydrothermal [4], chemical vapor deposition [5], etc. [6,7]), doping with metals [8–10] and non-metals [11,12], preparing composites with other semiconductors and/or metals [13–16], influencing the preferential orientation of the crystal structure [17,18] and synthesising ZnO with various morphologies [19,20].

During a photocatalytic process, the mineralization of pollutants is carried out by highly reactive free radicals generated on the surface of semiconductors. As such, a considerable amount of the semiconductor particle, that is, the interior portion, cannot participate significantly in the catalytic process. Consequently, the preparation of hollow semiconductors has gained considerable attention because of the following advantages:

i. There is a possibility to attain better photocatalytic performance with hollow structures than with solid structures because

* Corresponding author at: Department of Applied and Environmental Chemistry, University of Szeged, Rerrich tér 1, H-6720 Szeged, Hungary.
** Correspondence to: Institute of Physical Metallurgy, Metal Forming and Nanotechnology, University of Miskolc, Miskolc-Egyetemváros, C/1 108, H-3515 Miskolc, Hungary.
E-mail addresses: pzsolt@chem.u-szeged.hu (Z. Pap), hernadi@chem.u-szeged.hu (K. Hernadi).

https://doi.org/10.1016/j.jece.2022.107655
Received 2 November 2021; Received in revised form 28 March 2022; Accepted 1 April 2022
Available online 4 April 2022

photocatalytic reactions inherently take place at the interface of solid and liquid phases [21,22].

ii. The cavity in hollow structures decreases the apparent density of particles, which can facilitate their flotation in case of application in suspension of the photocatalyst [23].
iii. The mechanical properties (tensile strength, stiffness, etc.) is expected to be significantly reduced due to the low density. Literature data highlighted that the mechanical strength of the hollow materials can be preserved, especially in the case of hollow spheres [24].
iv. Higher economic feasibility can be achieved because the degradation efficiency to mass ratio is increased [25–27].
v. These materials can possess enhanced light harvesting capabilities through the constructive interference of light waves in the cavity [28].

Generally, a spherical template is applied to attain hollow morphology by its subsequent removal through calcination [29]. In recent years, due to the development of carbonaceous spheres prepared from glucose, they have become popular templates [30]. The formation of spheres is based on the sequential reduction of the carbohydrate in solvothermal conditions. In the case of ZnO there are few publications, where carbon spheres (CSs) were used to prepare hollow structures [31–33]. It was established that the formation of the ZnO layer is due to the polar interaction with the functional groups (-OH, =O, -COOH) on the surface, originating from the incomplete reduction of the surface of CSs [33]. Considering the simplicity and the mechanism of formation of spheres, other carbohydrates should also show potential to utilized for the preparation of CS templates. In our previous publication, a low-cost method was applied to prepare similar carbon spheres from sucrose, which were used as a template to synthesize hollow TiO_2 spheres. This way, the photocatalytic efficiency of TiO_2 spheres could also be improved [28]. This made the method more versatile and further reduced cost of materials. To the best of our knowledge such type of CSs was not applied to prepare ZnO hollow spheres (ZnO-HSs). Hence, the present study aims to evaluate the applicability of sucrose-derived CSs in comparison with the already existing synthesis methods involving its glucose-derived counterparts.

The deposition of noble metals is another technique that can greatly enhance the photocatalytic activity of ZnO [34]. The most common metals used are Ag [6], Au [35], Pd [36] and Pt [37]. The beneficial effect of noble metal nanoparticles lies within the fast transfer of photogenerated electrons to the metal phase. Consequently, this stabilises charge separation and decreases the probability of the recombination of electron–hole pairs [38]. There are numerous examples where ZnO were synthesized in composite with noble metals [38,39]. The improvement by noble metal deposition, depends on various aspects of the noble metal (crystallite size, morphology, etc.) [40]. The concentration of the noble metal in composite should be carefully chosen, because of two main reasons. One is the economic aspect of the materials, as usually the noble metal affects the synthesis cost predominantly. The other consideration involves the electron-hole separation process. As above a certain concentration the metal could facilitate the recombination, if the electronic transitions become favoured between the defect states of the semiconductor by the high surface density of conductive metal particles. Based on the literature, 1%wt or sometimes even less amount of noble metal is sufficient to improve the photoactivity of the semiconductor [41–43]. However, the photocatalytic evaluation of hollow structures in these composites are still scarce. Thus, in the present study both aspects were addressed (hollow spherical morphology and with the effect of noble metal deposition).

Most commonly, methyl orange, methylene blue and phenol are used as pollutants to determine the photocatalytic activity of ZnO in the literature. For better comparison with the literature the photocatalytic activity of ZnO samples prepared in this work was thoroughly investigated using phenol, diuron and ibuprofen. All of these model pollutants proved to be stable compounds, and their toxicity in the environment can be observed even at low concentrations.

2. Materials and methods

2.1. Reagents and materials

For the experiments, the following materials were used without further purification:

- ZnO precursors: zinc acetylacetonate ($ZnAA_2$, $Zn(C_5H_7O_2)_2$, 99.99%, Alfa Aesar, Germany), zinc acetate dihydrate ($ZnAc_2$, $Zn(C_2H_3O_2)_2$•2 H_2O, 99.98%, VWR International, Hungary), zinc chloride ($ZnCl_2$, >99%, Alfa Aesar, Germany).
- Solvents: absolute ethanol (EtOH, 100%, Molar Chemicals, Hungary) and ultrafiltered water (MQ, conductivity 77 $\mu S \bullet cm^{-1}$).
- For the preparation of CS templates: ordinary table sugar (sucrose, Magyar Cukor Zrt., Koronás™, Hungary) as carbon source, NaOH (>98%, Molar Chemicals, Hungary), MQ water.
- For noble metal deposition: hydrogen tetrachloroaurate(III) hydrate ($HAuCl_4$.4 H_2O, 99.99%, Sigma-Aldrich, Germany), hydrogen hexaplatinate (H_2PtCl_6; 99.9%, Sigma-Aldrich, Germany) trisodium citrate dihydrate (ACS, 99.0%, Sigma-Aldrich, Germany), sodium borohydride ($NaBH_4$, purum ≥96%, Sigma-Aldrich, Germany).
- Compounds used as model pollutants for photodegradation were ibuprofen sodium salt (99.99%, Merck KGaA, Germany), diuron (99.99%, Merck KGaA, Germany) and phenol (analytical grade, Spektrum 3D, Hungary).

2.2. Synthesis of carbon sphere templates

The hydrothermal synthesis of CS templates was carried out according to our recent publication [28] as follows. In a PTFE-lined autoclave, a 0.15 M water-based solution of sucrose was prepared (V_{fill}/V_{total} = 29%) and the pH was set to 12 using a 2 M NaOH solution. The as-prepared solution was subjected to hydrothermal treatment at 180 °C for 12 h. The obtained black precipitate was separated by centrifugation and washed with 100% acetone several times to remove residual organic contaminants formed during synthesis. This was followed by a drying step in air at 40 °C for 24 h. Then, the dark brown product was collected and ground to obtain the CS powder.

2.3. Synthesis strategies for the preparation of ZnO HSs

Two synthesis methods were applied to prepare a ZnO coating on the CS templates: chemical impregnation and solvothermal method.

During chemical impregnation, 200 mg of CSs was suspended in 60 mL of 99.3% (v/v) ethanol under vigorous magnetic stirring, in which 50 mmol of Zn precursor ($ZnAc_2$, $ZnCl_2$, $ZnAA_2$) was dissolved. The mixture was ultrasonicated continuously for 24 h. The aged solution was centrifuged to separate the impregnated CSs, followed by a drying step at 40 °C for 24 h. The as-prepared samples were calcined at 500 °C under continuous airflow to eliminate the CS templates through oxidation, resulting in crystalline ZnO. For this purpose, a Thermolyne 21,100 tube furnace was used applying 5 $°C \bullet min^{-1}$ heating rate with constant air supply (30 $L \bullet h^{-1}$).

During solvothermal synthesis, 15.5 mmol of Zn precursor and 300 mg of CSs were dissolved in 196 mL of 99.3% (v/v) ethanol and stirred for 1 h. These values were calculated according to the theoretical ZnO: CS mass ratio of 12:1. The reaction mixture was transferred to a PTFE-lined autoclave (V_{fill}/V_{total} = 70%) and subjected to solvothermal treatment at 180 °C for 12 h. The resulting solid samples were washed three times with 65%, 45%, and 20% (v/v) ethanol–water mixtures. The materials were then dried, calcined and ground the same way as described in the previous paragraph. The weight ratio of ZnO to CSs was fine-tuned to obtain regular hollow spheres and the samples with the

following ratios were further synthesized 10:1, 9:1, 7.5:1, 6:1 and 5:1. A schematic representation of the two synthesis methods is shown in Fig. 1.

A reference material was also fabricated consisting of solid ZnO spheres with average diameters equal to those of the hollow spheres described in the previous paragraphs as follows: a precursor mixture of 20% $ZnAc_2$ and 80% n/n $ZnAA_2$ was dissolved in 99% v/v ethanol-water mixture in 68 mmolar concentration and stirred for 40 min. Diethanolamine was added to the mixture in 3:1 molar ratio of diethanolamine:total zinc precursor and stirred for another 40 min. Later, the mixture was transferred to a PTFE-lined autoclave and subjected to solvothermal treatment at 180 °C for 12 h. The purification process was identical to that of the hollow spheres' and it was also calcined in the same conditions.

2.4. Noble metal deposition on ZnO HSs

Following the investigation of various ZnO synthesis methods, the one resulting in regular spherical morphology was selected for noble metal deposition. The following synthesis procedure was applied to deposit 1 wt% gold or platinum nanoparticles onto the surfaces of ZnO HSs: 198 mg of ZnO HSs was suspended in 22 mL of MQ water, to which 1.563 mL of trisodium citrate (0.063 mM) was added under vigorous stirring for 30 min. Then, 0.4 mL of $HAuCl_4 \bullet 4\ H_2O$ (25.4 mM) or 0.1625 mL of H_2PtCl_6 (31.3 mM) was added to the system. The chemical reduction of noble metal precursors was carried out using 0.5 mL of precooled (T ~ 0 °C) $NaBH_4$ (0.15 M) solution, which was stirred for another 30 min. The as-prepared Au and Pt ZnO-HS composites were separated by centrifugation from the suspension, then washed with MQ water three times, dried at 40 °C for 24 h and ground in an agate mortar.

2.5. Characterization

A Rigaku Miniflex II type diffractometer was used for X-ray diffractometry measurements (XRD, Shimadzu 6000) that was equipped with a graphite monochromator. The instrument was operated with Cu-Kα radiation (λ = 1.5406 Å) between 20 and 80 2θ°, applying 0.02° steps and $1^\circ \bullet min^{-1}$ scan speed. Mean crystallite sizes were estimated by 3 different methods, that is, the Scherrer equation, the Williamson-Hall analysis (W-H) [44] and the size strain plot (SSP). Each diffraction peak was fitted with a pseudo-Voigt function in OriginPro 2017. Other equations were also used as follows:

i.) Correction for instrumental broadening:

$$\beta_{hkl} = \left[(\beta_{hkl})^2_{Measured} - (\beta_{hkl})^2_{Instrumental}\right]^{\frac{1}{2}} \quad (1)$$

ii.) Scherrer equation:

$$D = \frac{K \times \lambda_x}{\beta_{hkl} \times cos\theta} \quad (2)$$

iii.) W–H equation:

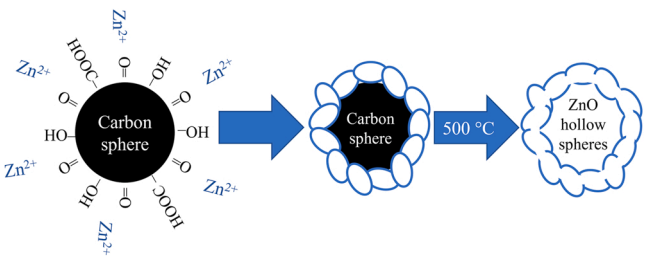

Fig. 1. Schematic image of the synthesis strategy applied in this work to prepare ZnO hollow spheres.

$$\beta_{hkl} \times cos\theta = \frac{K \times \lambda_x}{D} + 4 \times \varepsilon \times sin\theta \quad (3)$$

iiiv.) Size–strain equation:

$$(d_{hkl} \times \beta_{hkl} \times cos\theta)^2 = \frac{K}{D} \times \left(d_{hkl}{}^2 \times \beta_{hkl} \times cos\theta\right) + \left(\frac{\varepsilon}{2}\right)^2 \quad (4)$$

where β_{hkl} is the full width at half maximum, θ is the Bragg angle, d is the distance between adjacent planes with the Miller indices (hkl) (calculated from the Bragg equation, i.e., λ = 2d sinθ), D is the crystallite size, K is the shape factor (0.9), and ε is the crystal strain.

For some samples, the texture coefficient was also calculated using the three main reflections of ZnO (100), (002), (101) and reference diffraction data available at [45]. The equation used for the calculation of texture coefficient was the following [46]:

$$TC_{hkl} = \frac{\frac{I_{(hkl)}}{I_{0(hkl)}}}{\frac{1}{N} \times \sum_N \frac{I_{(hkl)}}{I_{0(hkl)}}}, \quad (5)$$

where TC_{hkl} is the texture coefficient of the (hkl) plane, I is the measured intensity, I_0 is the standard intensity of the corresponding plane, N is the number of reflections considered. TC values are equal to 1, if the structure is close to that of bulk ZnO.

The diffuse reflectance spectra (DRS) of the samples were obtained using a Jasco-V650 UV–Vis spectrometer with an integration sphere (ILV-724). The measurements were taken in the wavelength range of 250–800 nm using $BaSO_4$ as the reference. Band-gap energies were calculated by the Kubelka-Munk equation and Tauc plot representation. Possible electron transitions were estimated by the first derivative of the DRS. The room-temperature photoluminescence (PL) emission spectra of the samples were recorded at 350 nm excitation wavelength using a Horiba Jobin Yvon Fluoromax-4 type spectrofluorometer and a 350 nm cut-off filter.

The surface of the ZnO samples were studied using Fourier transform infrared spectroscopy (IR) with a Jasco 6000 spectrometer in the 400–4000 cm^{-1} range applying 4 cm^{-1} spectral resolution.

The morphology of the samples was analyzed by a Hitachi S-4700 Type II scanning electron microscope (SEM) and a FEI TECNAI G2 20 X-Twin type transmission electron microscope (TEM). The micrographs were further evaluated to determine the diameters and distribution of diameters in the ImageJ software.

2.6. Assessment of photocatalytic activity

The photocatalytic efficiency of the ZnO samples was evaluated by the decomposition of Na-ibuprofen ($C_{0,ibuprofen}$= 0.1 mM), diuron ($C_{0,diuron}$= 0.1 mM) and phenol ($C_{0,phenol}$= 0.1 mM). The four hour measurements were carried out under UV irradiation (6 × 6 W fluorescent lamps, Vilber-Lourmat T-6 L UV-A, $\lambda_{max} \approx 365$ nm) with a distance between the reactor and lamps 5 cm. For a typical experiment, 100 mL of a solution containing the pollutant and the catalyst ($C_{catalyst}$ =1 $g \bullet L^{-1}$) was prepared. The mixture was sonicated in the dark for 10 min to ensure adsorption-desorption equilibrium. The suspension was transferred to Pyrex® glass tube reactor with a thermostatic jacket and 2.5 cm inner diameter. During the experiments, constant temperature (25 °C, by circulating water in the thermostatic jacket using an ultra-thermostat), magnetic stirring (400 rpm) and the dissolved oxygen concentration (by bubbling with air at 30 $L \bullet h^{-1}$) were maintained.

The concentrations of the model pollutants were measured with high performance liquid chromatography (HPLC). The device consisted of a Merck Hitachi L-7100 low-pressure gradient pump equipped with a Merck-Hitachi L-4250 UV–Vis detector ($\lambda_{detection}$ = 210 nm for phenol, 214 nm for ibuprofen and 254 nm for diuron). A 50% (v/v) ethanol-water mixtures were used as eluent for phenol and ibuprofen, respectively 70% (v/v) for diuron. To investigate the reusability of ZnO hollow

spheres, the phenol degradation experiments were repeated two additional times.

The total organic carbon content was measured at the end of the photocatalytic tests after 4 h of irradiation. The equipment used was an Analytik Jena N/C® 3100 apparatus with NDIR detector. The furnace temperature was 800 °C and 1.0 mL samples were injected. The measurements were made in triplicate.

3. Results and discussion

3.1. Morphological characterization of ZnO HSs

As mentioned before, one of the main scopes of the present research is to examine the applicability of sucrose-derived CSs in comparison with the already existing methods to prepare ZnO with hollow spherical morphology. In general, the surface of carbon spheres is not completely reduced, and residual hydroxyl, carbonyl and carboxyl groups are present. Due to the affinity of Zn^{2+} to coordinate with these groups, it can be utilized to prepare carbon-ZnO composites via chemical impregnation [47,48]. Consequently, the removal of carbon templates through oxidation promotes the formation of ZnO from the zinc ions bound on the CSs' surface. The difficulty is to ensure that the binding of zinc is stable enough so that it does not redissolve into the liquid phase. This could be overcome in the solvothermal method as the high temperature could facilitate the decomposition of the precursor and the formation of ZnO.

Carrying out the synthesis of ZnO via chemical impregnation resulted in only a minuscule amount of solid material. In the case of $ZnCl_2$ no material was recovered after calcination at all. On the contrary, the solvothermal method resulted in yields close to 100%. The results of morphology measurements are shown in Fig. 2. The samples contained mainly sub-micrometer-sized rod-shaped or larger irregular crystals. However, when $ZnAA_2$ precursor was used, some spherical particles could also be observed. One explanation for the general absence of spherical particles could be that the crystal formation took place alongside the particles, or that the adhesion of the formed crystals to the CSs' surface was not sufficient. Such an example can be seen in Fig. S1, which shows a SEM micrograph of a sample synthesized using $ZnAc_2$ before calcination. The surface of CSs could not bound sufficiently zinc ions when the solutions of Zn-containing salts were used. In the case of glucose-derived CSs used in the literature using $ZnAc_2$ and $ZnCl_2$ the impregnation of the surface occurred relatively successful[31–33]. The used purification method for the CSs has already proven in our previous research that efficiently removes the by-products of the carbonization process [28]. This results in less functional groups on the surface which could participate in polar-polar interactions. In consequence no strong polar-polar interaction can occur between the surface of the CS and the polar Zn salts or even ZnO.

Even though using $ZnAA_2$ during chemical impregnation did not yield spherical particles, its application during solvothermal synthesis resulted in the sample containing mainly spherical particles. Yet, the spheres were aggregated, and the average size was 10 times higher than

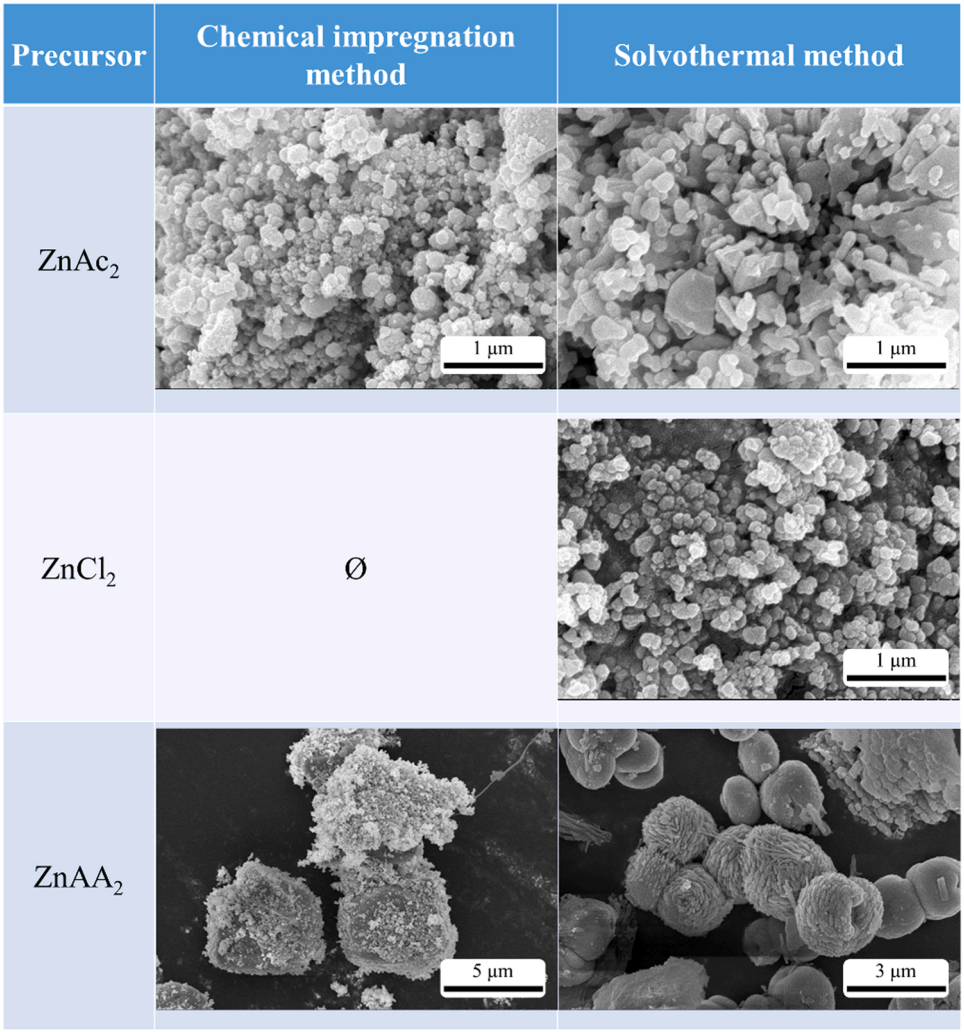

Fig. 2. SEM micrographs of samples synthesized by chemical impregnation and solvothermal method.

that of the CS templates. Thus, this sample was selected for further investigation to optimize and increase the ratio of spherical particles. The mass ratios of ZnO to CSs were varied (10:1, 9:1, 7,5:1, 6:1, 5:1), but the concentration of $ZnAA_2$ was kept constant throughout the experiments. These samples were hereinafter referred to as "ZnO-HSs-*$ZnAA_2$: CSs mass ratio*". The SEM micrographs of these samples are presented in Fig. 3. Spherical particles were achieved in each case regardless of the applied $ZnAA_2$:CS mass ratio, but alongside the spheres some damaged structures could always be observed. This most probably can be attributed to that the ligand (acetylacetonate) can participate in non-polar interaction with the surface of the CS. As the concentration of the templates increased, less spherical particles were formed. At the same time, the size of the spheres also increased, and more irregular small crystals were formed. At a lower concentration (e.g., at a 6:1 ratio), some spherical cavities could be observed at the surface of agglomerated particles, with sizes corresponding to those of CSs (~500 nm).

The presence of smaller irregular particles suggests that the nucleation of ZnO occurs in both the solvent phase and at the surface of the CSs. For ZnO-HS-10:1, the average diameter of spheres was ~800 ± 80 nm based on the SEM micrographs. Based on the broken spheres in the figures, the formation of the hollow morphology could be confirmed due to the presence of cavities. In addition, the least amount of irregular crystals wwere observed in this sample. Assuming that the diameter of the cavity in the hollow spheres are equal to the average diameter of CSs, the thickness of the ZnO shell is ~150 nm. The actual values determined based on TEM micrographs (Fig. 4) show that the diameter of the cavity varied between 350 and 450 nm and the thickness of the shell was 110–170 nm. The slightly smaller cavity value can be attributed to the sintering process. The ZnO-HS-10:1 sample was selected for noble metal deposition in further experiments, and hereinafter it will be denoted as "ZnO-HS". As a reference, solid ZnO spheres were also fabricated (denoted as "ZnO-SS") using a similar synthesis method, which had the same average diameter.

3.2. Structural and optical characterization of ZnO-HSs

The crystal structure and optical properties of ZnO-CS, ZnO-HS and noble metal-containing ZnO-HS composites were examined by XRD, IR and DRS measurements. Even though CSs were applied as templates, they could also directly influence the growth of ZnO crystals.

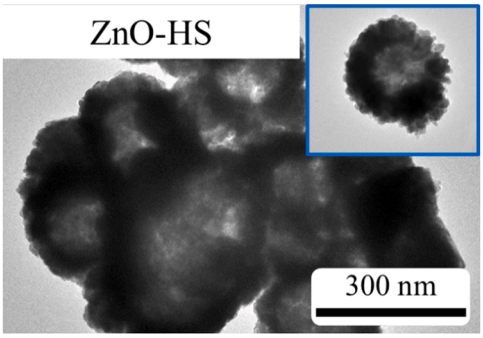

Fig. 4. TEM micrograph of ZnO-HS synthesized with tuned ZnO:CS weight ratio.

The XRD patterns are shown in Fig. 5. The main diffraction peaks corresponding to the wurtzite crystal structure were identified according to the reference diffraction data (JCPDS 36–1451) at 2θ°: 31.74, 34.39, 36.21, 47.54, 56.59, 62.89, 66.38, 67.98, 69.11 [45]. The presence of noble metals in the composite materials was also confirmed by identifying the corresponding diffraction peaks at 38.14 and 44.32 2θ° values for Au (JCPDS 04–0784) [49], and at 39.70 2θ° values for Pt (JCPDS 04–0802) [50]. Based on the XRD data, the mean crystallite sizes were determined using three methods (Scherrer, W-H and SSP) and the results are presented in Table 1. Preparing ZnO via solvothermal method resulted in a structure with high preferential orientation for the (002) plane. To better quantify this aspect, texture coefficients (TC) were calculated for the three main diffraction peaks corresponding to the (100), (002), and (101) crystallographic planes. Based on the literature, the W-H and SSP methods are one of the most appropriate methods to determine the actual crystallite size, because the broadening resulted from the crystal strain is also considered. In the present case this is well exemplified, as the results calculated by the W-H and SSP methods are greater than those calculated by the Scherrer equation. This difference was expected, as the Scherrer crystallite size was in the range of 14–18 nm. At such a low crystallite size, the strain produced more distortions, which in turn caused broadening.

An increase in crystallite size was observed between the non-calcined ZnO (ZnO-CS, 20.50 nm) and the calcined (ZnO-HS, 26.24 nm). This is

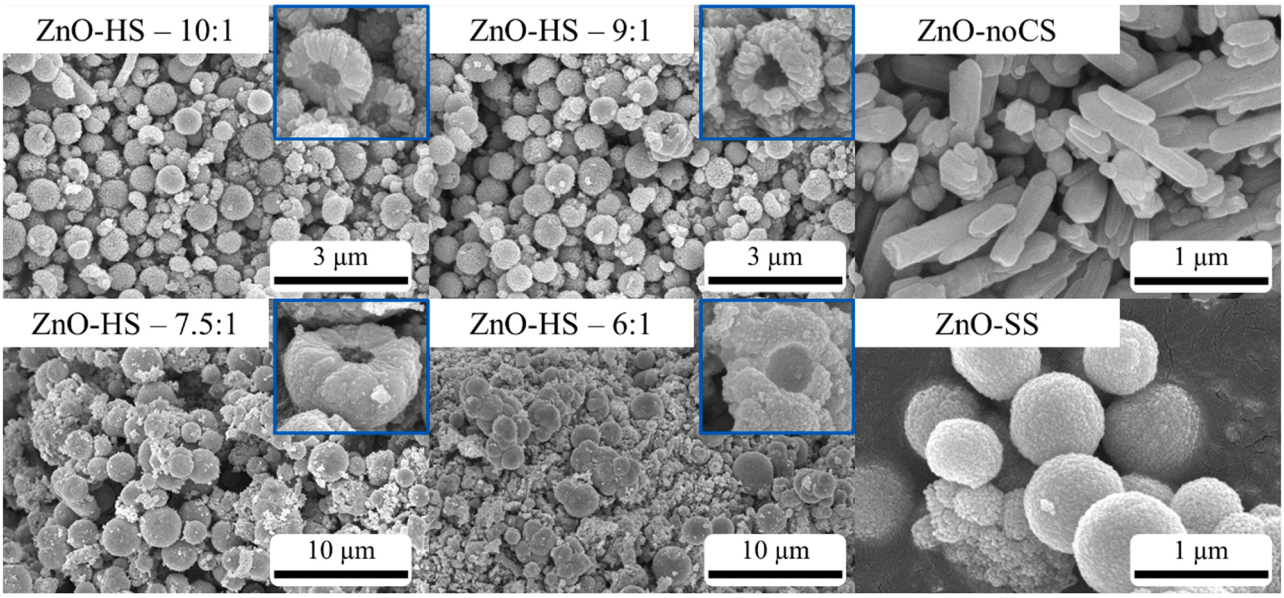

Fig. 3. SEM micrographs of samples synthesized with different $ZnAA_2$:CS mass ratios and reference samples (ZnO solid spheres (SS) and ZnO samples synthesized without CSs (noCS)). As the ratio increased, more spherical particles were formed.

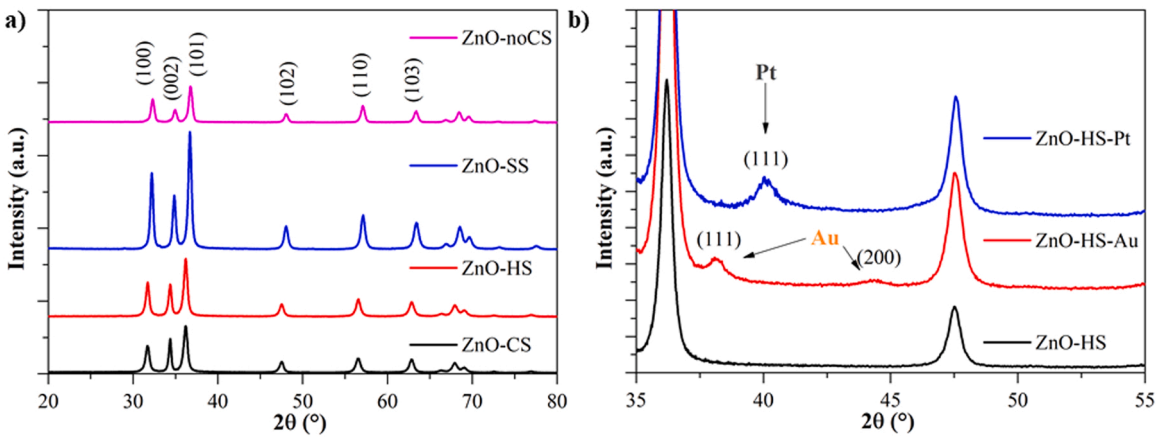

Fig. 5. XRD patterns of ZnO samples (a) and ZnO/noble metal composites (b).

Table 1
Crystallite size calculated by Scherrer equation, W-H and SSP methods and TC values of the ZnO samples.

Sample	Mean crystallites size (nm)			TC		
	$d_{Scherrer}$	d_{W-H}	d_{SSP}	(100)	(002)	(101)
ZnO-noCS (reference)	16.68	17.75	17.18	0.97	1.12	0.93
ZnO-SS (reference)	17.14	23.45	20.45	1.05	1.06	0.89
ZnO-CS	14.48	20.50	17.25	0.84	1.41	0.75
ZnO-HS	15.59	26.24	20.54	0.95	1.22	0.83

well explicable by the sintering phenomenon, resulting from the high temperature applied during CS removal. As mentioned before, the ZnO-noCS used as reference (synthesized without CSs) contained strongly oriented crystals. The cause of this preferential orientation is described in our previous publications [51]. This aspect is well-revealed in the TC values showing a strong preferential orientation for the (002) crystallographic plane. Surprisingly, the addition of CSs and the change of morphology did not induce significant changes in the overall preferential orientation. Consequently, the preferential crystal growth along the (002) plane was not affected by the template, only the morphology. The change in crystallite size of the calcined sample confirmed that sintering had occurred. This process not only involves the fusion of particles, but also the facilitated rearrangement of the structure to a more stable form.

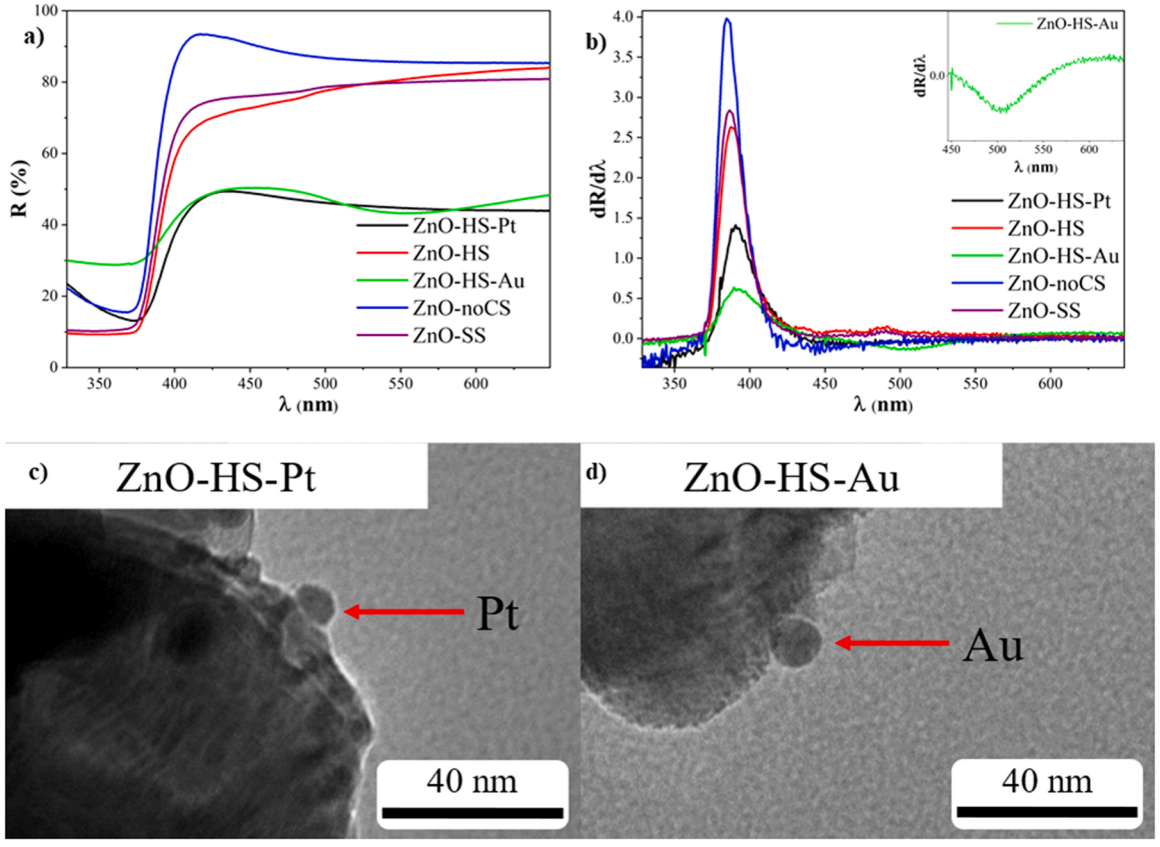

Fig. 6. Diffuse reflectance (a), first derivative diffuse reflectance spectra (b) of ZnO samples and their composites and TEM micrographs of ZnO-HS-Pt (c) and ZnO-HS-Au (d).

Consequently, the calcination process decreased the preferential orientation. As a result, the TC values after calcination were closer to 1 than those before calcination. The degree of preferential orientation was practically halved after the CS removal process. The crystallite sizes of the noble metals were determined only by the Scherrer equation, because the data from the XRD measurements was not sufficient to calculate reliable results by the W-H and SSP methods. The crystallite size showed very close values, 9.57 nm for Au and 9.53 nm for Pt nanoparticles. The TEM micrographs (Fig. 6**c** and 6**d**) of the composites confirmed the presence of ~10 nm sized particles on the HS surface corresponding to the size of the noble metal particles[40]. The chemical deposition process did not result in any observable change in the crystal structure and the crystallite size remained unchanged.

The light absorption proprieties of the samples were investigated by DRS measurements (Fig. 6). The decrease of reflectance in the UV-range is typical of semiconductor oxides [52]. Significant differences could be observed in the reflectance values in the visible region between the composite and pure ZnO samples. Au and Pt absorb light in the visible range, which is in good accordance with the samples having a grey (ZnO-HS-Pt) or purple (ZnO-HS-Au) color. The band gap energies of pure semiconductor materials can be determined by the Kubelka-Munk method; however, for composite materials the spectra of different components superimpose on each other. Consequently, the first order derivatives were used to determine the band-gap energies of the noble metal-containing samples. Applying such an approach also gives insight regarding the excitability of photocatalysts. The band gap values for both pure ZnO (ZnO-noCS and ZnO-HS) samples were 3.19 respectively 3,22 eV, which is equivalent to 388 nm wavelength of radiation. This value is in the typical range of excitability for ZnO-based photocatalysts, which is in the UV-A range [53]. The noble metal deposition induce a slight red-shift in the band gap energies of the composites (3.17 eV), which were identical for both Au- and Pt-containing samples. The localized surface plasmon resonance specific for gold nanoparticles could be observed in the derivative spectrum of ZnO-HSs-Au (inflection point at 542 nm).

The band gap tails were calculated for each sample, as it gives information about the defect state energy levels in the semiconductor. Defect states can directly contribute to the stabilization of electron–hole pairs [54]. The band gap tail energy, also called Urbach energy was determined according to the publication of P. Norouzzadeh et al. [55]. By comparing the Urbach energies (E_U) of pure ZnO samples (ZnO-noCS, -SS, -HS), no significant difference was observed, so the use of CS templates did not result in any noticeable changes in the band structure. However, due to the noble metal deposition, a threefold increase was observed in the band tail energies. The source of these defect states could be the corrosion by the other chemical species involved (citrates and chloride ions) during deposition apart from the metal nanoparticles themselves.(Table 2).

The photoluminescence (PL) spectra of the samples are shown in Fig. 7. PL is an effective way to study the electronic, optical and photochemical proprieties of semiconductor photocatalysts. In the UV and near-UV region should be the emission of near band edge (NBE) transition of ZnO as a result of the exciton recombination. Generally, this is also accompanied by a broad emission in the range of 450–750 nm. It has been established that in this region takes place the emissions due to defects states of the ZnO: blue-green emission in 480–550 nm, originated from the singly charged oxygen vacancies, yellow in 580–610 nm from doubly charged oxygen vacancies or zinc interstitials, the orange-red emission in 620–750 nm is proposed to be the defect complexes involving zinc vacancies or zinc interstitial complexes due to oxygen vacancies [56–58]. The yellow emission is the most common in pristine ZnO. Although the intensity of the PL emission is a widely used base for comparison between photocatalyst to explain the efficiency of the charge separation process, discussing the different emissions in relation to the other is more advised. In present case ZnO-CS presents the common NBE, centered at 391 nm, yellow emission (centered at 624 nm) and a slight orange-red emission at 646 nm, but the intensity of the defect emissions is obviously higher. This region is further presented in the supplementary material as Fig. S2. The effect can be attributed to the low oxygen level during synthesis and on the surface of the template. After calcination, the NBE is significantly reduced and the center is shifted to 411 nm. The yellow emission has become more intense and the same amount of shifting can be observed. This implies that the population of defect state is increased. In consequence the recombination pathway of the separated charges is also more probable to take place through the lower defect states. The oxidation of the carbon template could result in the removal of a portion of the oxygen atoms from ZnO, which would cause such an intense yellow emission. The noble metal deposition should reduce the recombination due to affinity of the metal phase to host the separated electron, which is well-reflected in the decrease of the intensity of NBE emission, but only for ZnO-HS-Pt composite, while in the case of ZnO-HS-Au defect emissions are reduced. Also a few nms of redshift of all the peak centers is observed. This implies a different preferential formation of semiconductor-metal junction for the metals towards ZnO. Likely, the Au nanoparticles visible range plasmon resonance levels are more energetically close to the electrons at the defect states [43,59,60], and vice versa Pt towards the band edge states [61–63]. An intensity increase is observable in the region where the blue-green and the orange-red emissions takes place. The most likely explanation is that, the reducing environment during noble metal deposition changed some of the defect states on the surface of ZnO-HS.

The surface of the samples was investigated by FTIR measurements, and the results are shown in Fig. 8. The intense band centered at 460 cm^{-1} was attributed to Zn–O stretching vibrations [64]. The typical absorption bands for adsorbed water and CO_2 were observed at 3435 cm^{-1} (stretching vibrations of O–H bonds) and between 2341 and 2361 cm^{-1}, respectively. ZnO-HSs showed a relatively narrow band at 1627 cm^{-1}, 1579 cm^{-1} and 1610 cm^{-1} which were attributed to the bending and stretching vibrations of the adsorbed water molecules [65]. No bands were observed that could be attributed to carbon–carbon bonds. This implies that the calcination procedure was successful in removing the carbon sphere templates.

3.3. Photocatalytic activity

The photocatalytic activity of ZnO-HS with or without noble metals and the reference materials (ZnO-noCS and ZnO-SS) were measured by the photocatalytic degradation of phenol, ibuprofen and diuron under UV light irradiation and the resulted degradation curves are presented Fig. 9. During the adsorption period (i.e., no irradiation was applied for 10 min) no significant concentration change (<0.5%) was observed for any of the investigated samples and model pollutants. Although publications studying the photocatalytic activity of ZnO hollow spheres are scarce, the results of few studies are presented in Table 3 for comparison.

The reference materials were compared to our previous results [51], because in the present work a calcination step was added to the original synthesis method of ZnO-noCS and ZnO-SS, in order to be comparable to the hollow structures. In general, calcination is included in the synthesis of ZnO to improve crystallinity. The precursors used in the syntheses contain some form of moiety. In consequence, the crystallization of ZnO rarely occurs in a direct chemical process, and the formation of $Zn(OH)_2$ is difficult to avoid. As such, the hydroxide groups can be removed by a

Table 2
Calculated band gap (E_g) and Urbach energy (E_U) values of the ZnO samples.

Sample name	E_g (eV)	E_U (meV)
ZnO-noCS (reference)	3.22	52
ZnO-SS (reference)	3.19	56
ZnO-HS	3.19	58
ZnO-HS-Au	3.17	232
ZnO-HS-Pt	3.17	240

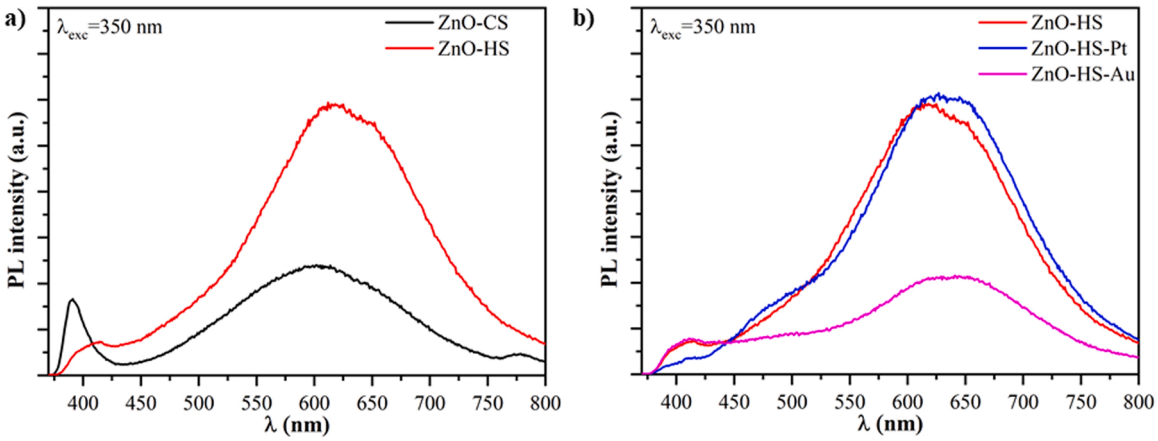

Fig. 7. PL emission spectra of the as-prepared samples recorded at 350 nm excitation wavelength for (a) ZnO-CS and ZnO-HS (b) comparison between ZnO-HS and its respective noble metal composites.

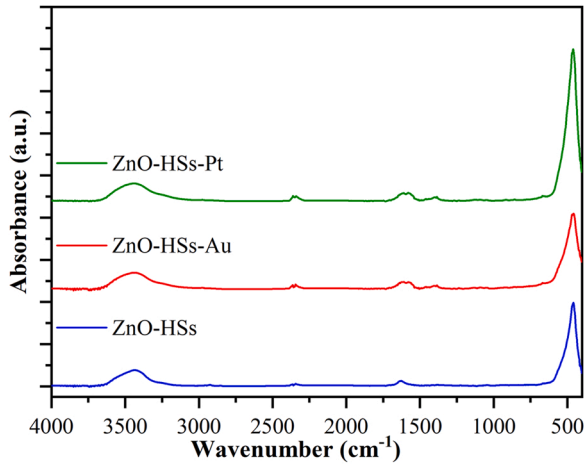

Fig. 8. FTIR spectra of the investigated photocatalysts.

high temperature thermal treatment that also improves crystallinity [66, 67]. In the present case, the effect is obviously the opposite. During the solvothermal synthesis the water content was low (0.7% in the solvent and the moiety of the precursors), which is required for the formation of ZnO, and the reaction mixture consisted mainly of organic compounds (ethanol and acetylacetonate ligand from the precursor). This was not completely removed from the sample. Most probably they were adsorbed on the surface or trapped at defect sites. The high temperature results in the oxidation of organic impurities to CO_2 and H_2O. These carbon-based impurities could also use up the loosely bound oxygen on the surface of ZnO during oxidation that are already prompt for desorption at high temperatures. This decrease in activity is higher for ZnO-noCS than for ZnO-SSs. This can be explained as follows. In ZnO-noCSs, the preferential orientation along the (002) plane is more prevalent, which has already been correlated with the photocatalytic activity of ZnO. If this orientation tends to result in crystal facets containing terminal oxygen, then the oxidation of carbon impurities could decrease the oxygen content along those facets. Subsequently, in the present case, calcination induces the oxidation of residual carbon impurities, reducing the oxygen-rich crystal facet, which in turn could reduce the photocatalytic activity.

The photocatalytic activity of ZnO-HS was compared to that of reference ZnO samples, and surprisingly, the degradation of phenol showed a 83% and a 132% improvement compared to that observed for ZnO-SSs and ZnO-noCS, respectively. This can be attributed to the fact that ZnO-HS retained much more from the original preferentially oriented structure. This was unexpected because this catalyst contained much more carbon-based materials (due to the presence of templates) than the references. Although it is worth noting that the carbon template is not as intercalated into the crystal structure as the impurities originating from the solvent and the precursor. Nonetheless, the relatively small thickness of the shell, which is composed of smaller crystals with gaps between them, can hardly obstruct the diffusion of oxygen during calcination.

The photocatalytic activity of composite materials was also compared to that of the base material (ZnO-HSs) to investigate the effect of noble metals. The apparent rate constants (k_{obs}) were determined for the ZnO-HSs and the respective noble metal composites (based on Fig. 10), which are presented in Table 4.

The composite photocatalysts performed much better than the base material, as k_{obs} increased 270% and 336% increases were observed during the degradation of phenol for Au and Pt composites and even higher increases for the other two model pollutants. After 4 h, both samples reduced the concentrations close to zero. The increase of photocatalytic activity by noble metal deposition is usually attributed to their electron acceptor role, facilitating the stabilization of separated electron–hole pairs and preventing recombination. The difference in photocatalytic activities due to the presence of Au and Pt nanoparticles can be attributed to two aspects. One is that the plasmon resonance of Au nanoparticles is in the visible range, while the plasmon resonance of Pt is at the high energy end of the UV spectrum. This makes the utilization of plasmon resonance during the photocatalytic process more probable for Au than that for Pt. The second aspect is that gold nanoparticles have higher conductivity for electrons than platinum nanoparticles. Considering that the irradiation was in the UV range is the charge separation through conduction of electrons in the metal particles are more probable.

The photocatalytic activity of the samples was investigated also for diuron and ibuprofen. The base material and reference materials were considerably less effective in the degradation of diuron and ibuprofen compared to their efficiency in the degradation of phenol. This is explicable by the fact that this organic molecule is more stable, larger and can produce more intermediates [68–70]. On the other hand, the composites still managed to degrade the model pollutants in 4 h. In contrary to the degradation of phenol, ZnO-HSs-Pt was slightly better than ZnO-HSs-Au, especially for diuron. The slightly better photocatalytic activity towards diuron compared to ibuprofen could be explained by the fact that diuron contains chlorine substituents, which can interact more easily with the (002)-oriented surface [68]. The PL measurements suggested that Pt can improve the electron-hole separation more efficiently at the near band edge than Au, which could explain the better activity of Pt composite compared to Au. As such from

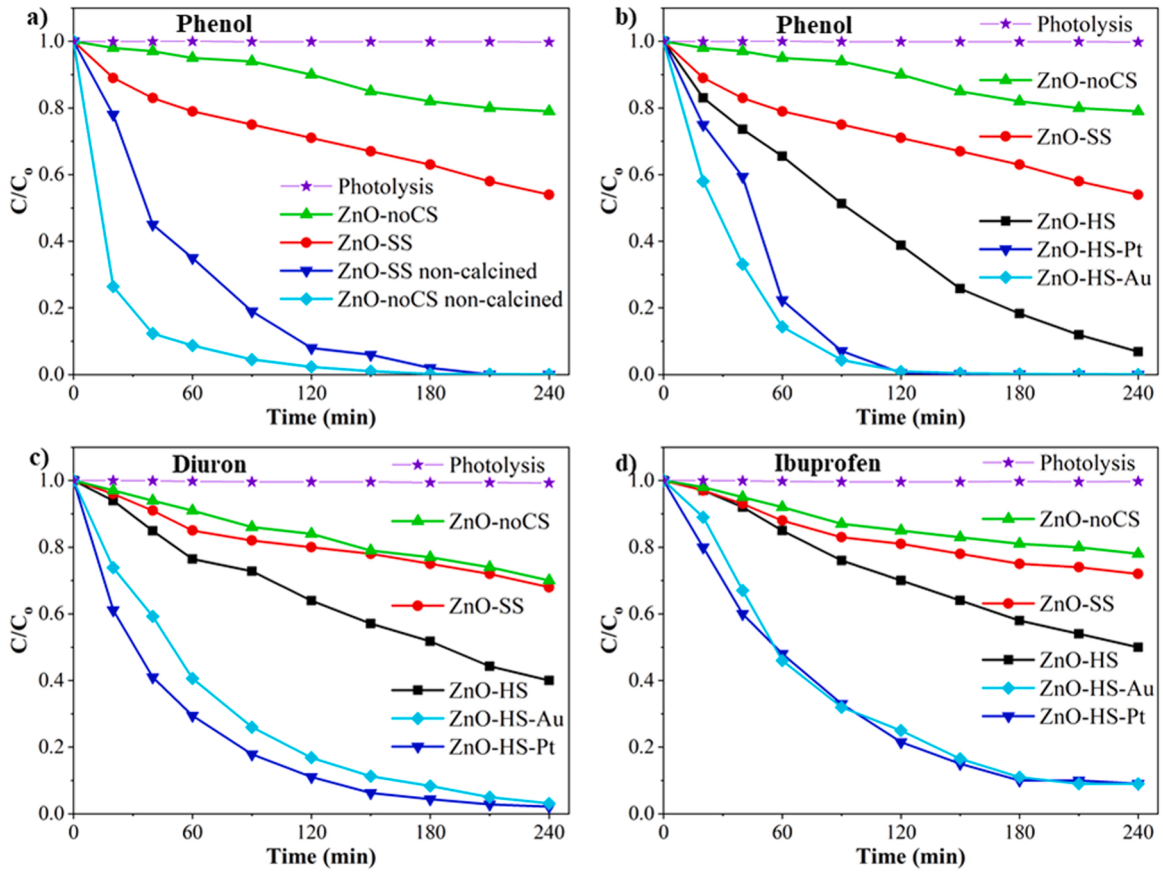

Fig. 9. Degradation curves of model pollutants using the as-synthesized ZnO and composite samples under UV irradiation: a) comparison of the reference materials before and after calcination, b) phenol, c) diuron, d) ibuprofen ($C_{0,phenol} = C_{0,diuron} = C_{0,ibuprofen} = 0.1$ mM, $C_{catalyst} = 1$ g/L).

Table 3
The observed photocatalytic degradations of several Hollow ZnO spheres in the literature.

Catalyst	Conditions					Reference
	Catalyst concentration (g/L)	Model pollutant	Concentration of model pollutant (mM)	Degradation time (h)	Conversion (%)	
Reduced graphene-oxide/ZnO	0.2	Methylene blue	0.01	1.5	99	[66]
ZnO	0.5	Congo Red	0.02	1.5	85	[48]
Au/ZnO	1.7	Methylene blue	0.053	0.33	73.7	[31]
Au/Graphene/ZnO	Catalyst on substrate	Methylene blue	0.01	1	56	[67]
ZnO	1	Rhodamine B	0.042	0.83	99	[32]

practical point of view Pt deposition could improve more efficiently the photocatalytic activity than Au.

The hollow morphology was proven to promote internal reflection and facilitate a more efficient light harvesting in TiO_2. For such phenomenon the absorptivity of the material, the thickness of the shell and the diameter of the internal cavity should be considered. Regarding this issue, existing literature reporting on ZnO thin films of similar thickness as the diameter of ZnO spheres prepared in this work can be utilized [71, 72]. It is well-established that thin films of ZnO have high transmittance in the visible range, but in the UV range (< 400 nm) they have poor transmittance (<10%) even at low thickness values (<100 nm) [73]. Consequently, it was presumed that UV light did not participate in the light harvesting process through internal reflection. Another requirement for the visible light to be intensified through constructive interference is that the internal diameter of the spheres should be an integer multiple of the wavelength. The diameter of the cavities in the hollow ZnO spheres presented in this work was 350–450 nm, which would only allow this phenomenon to occur in the UV range. Subsequently, the enhancement of photocatalytic activity by internal reflections was ruled out for these samples.

The degradation of organic pollutants can result in various intermediates before reaching the complete oxidation. Some of these intermediates can be more toxic and more stable than the original compound. One representative example is the degradation of phenol, which can form hydroquinone, resorcinol and catechol, which are all more toxic and hydroquinone is more stable than phenol. These intermediates were also detected in the chromatograms (Fig. S3). Ideally, the final reaction products of photocatalysis are CO_2 and H_2O, so the change in total organic content better reflects the efficiency of the photocatalytic degradation process. In Fig. 10 the TOC and phenol conversion values are presented after 4 h of degradation. As expected, the corresponding TOC values are smaller than the phenol conversion values. It also reveals that higher TOC removal can achieved with noble metal deposited ZnO. The TOC removal is significantly increased after the phenol conversion reaches 90%. Nonetheless, total mineralization occurs after 12 h and 6 h for ZnO-HS and ZnO-noble metal composites.

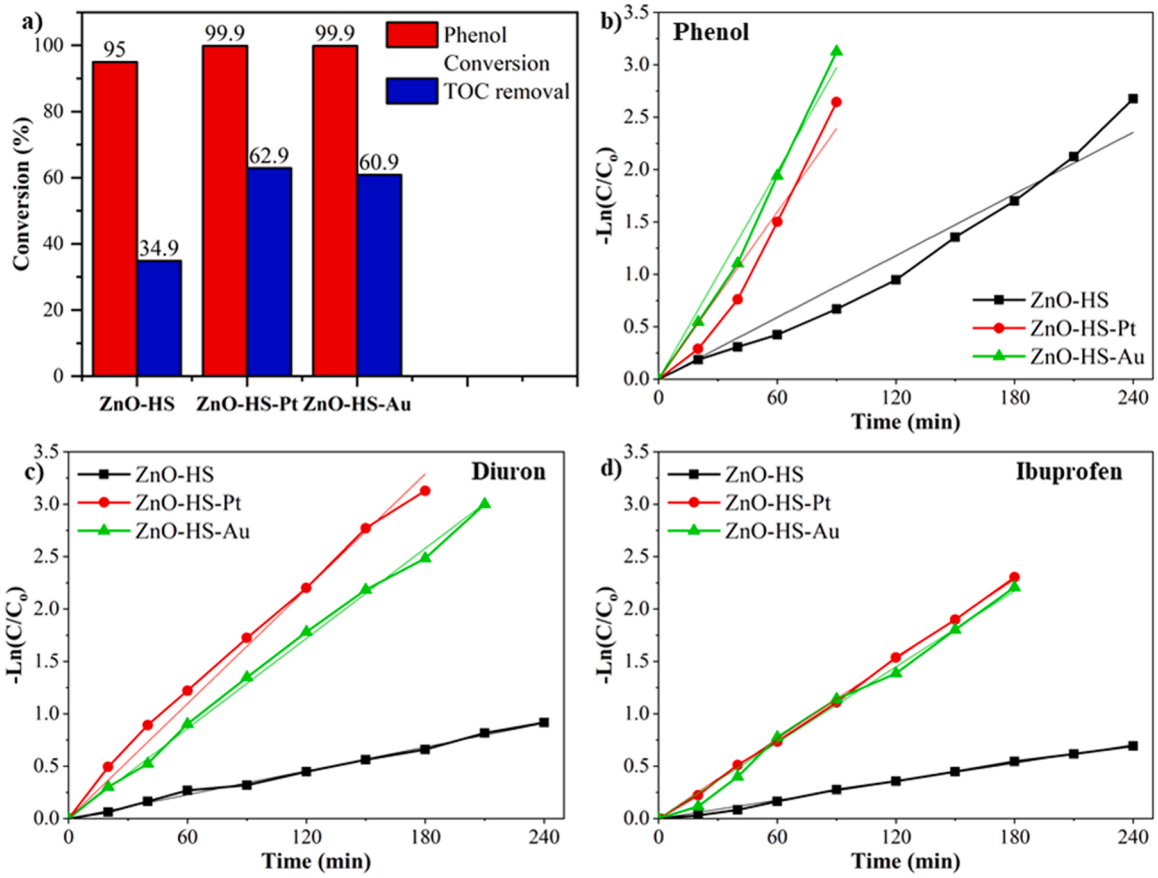

Fig. 10. Phenol conversion and TOC removal values (a), kinetic plots for phenol (b), diuron (c), ibuprofen (d) of ZnO-HS, ZnO-HS-Pt and ZnO-HS-Au samples.

Table 4
The calculated apparent rate constants determined for the as-prepared samples for the degradation of three model pollutants.

Sample name	k_{obs} (min^{-1})		
	Phenol	Diuron	Ibuprofen
ZnO-HS	9.81	3.79	2.93
ZnO-HS-Pt	26.57	18.27	12.68
ZnO-HS-Au	33.05	14.32	12.07

To sum up, based on the photocatalytic experiments, the hollow spheres were more efficient than the solid spheres and the template-free reference regardless of the model pollutant applied. The noble metal deposition successfully increased the photocatalytic activity of hollow structures at least twofold.

The reusability and stability of the base material (ZnO-HS) were investigated and presented in Fig S4. For this sample the phenol degradation experiment was carried out three times. The XRD and SEM measurements were repeated and the catalyst proved to be remarkably stable as they retained their crystal structure, morphology and photocatalytic activity. Additionally, the best performing catalyst, ZnO-HS-Pt, was further examined in simulated waste water conditions described in the Supplementary material (see Fig. S5).

4. Conclusion

Sucrose-derived carbon sphere templates were investigated in the synthesis ZnO hollow. Applying sucrose-derived CSs did not result in the formation of hollow structures when chemical impregnation was applied as the synthesis method. However, sucrose-derived CSs were successfully applied during solvothermal synthesis to prepare hollow ZnO spheres. The optimal conditions (10:1 ZnO:CS mass ratio) to obtain regular hollow spheres were identified. The removal of templates by calcination was confirmed by SEM and TEM measurements. For the reference materials the temperature applied during calcination resulted in the loss of the preferential orientation towards the (002) crystallographic plane. For the hollow structures, the preferential orientation was partially preserved due to the presence of the templates.

Au and Pt nanoparticles were successfully deposited onto the surface of HSs by chemical reduction, which was confirmed by XRD, TEM, PL and DRS measurements. The morphology and structure of ZnO remained unchanged, despite the presence of noble metals, the emission spectra of the composites showed that Pt enhances the charge separation in the UV range and Au reduces the recombination through the defect states.

The photocatalytic activity of the samples was investigated by the degradation of phenol, ibuprofen and diuron under UV irradiation. ZnO hollow spheres outperformed the reference materials by at least 70%. The presence of noble metals resulted in a remarkable 270% or greater increase in the apparent rate constants of the photocatalytic degradation, depending on the model pollutant used. Similar increases in efficiencies were observed both for Au and Pt nanoparticles. The catalysts were also reusable and stable during the reusability tests.

The higher efficiency of hollow ZnO samples was attributed to their preserved preferential orientation towards the (002) plane. In consequence, the implementation of sucrose-derived carbon spheres improved the photocatalytic activity of ZnO synthesized via the solvothermal method.

CRediT authorship contribution statement

Zoltán Kovács: Conceptualization, Visualization, Investigation, Writing – original draft preparation, Formal analysis. **Viktória Márta:**

Investigation, Data curation. **Tamás Gyulavári:** Investigation, Software. **Áron Ágoston:** Investigation, Visualization. **Lucian Baia:** Supervision, Reviewing and Editing. **Zsolt Pap:** Supervision, Visualization, Formal analysis. **Klara Hernadi:** Writing – reviewing and editing, Supervision, Resources.

Declaration of Competing Interest

The authors declare that they have no known competing financial interests or personal relationships that could have appeared to influence the work reported in this paper.

Acknowledgments

This study was financed by the National Research, Development and Innovation Office, Hungary NKFI-K-124212 project. Z. Kovács is grateful for the financial support of the NKFI-TNN-16–123631 project. Zs. Pap acknowledges the Bolyai János scholarship provided by the Hungarian Academy of Sciences.

Appendix A. Supporting information

Supplementary data associated with this article can be found in the online version at doi:10.1016/j.jece.2022.107655.

References

[1] P. Raizada, A. Sudhaik, P. Singh, Photocatalytic water decontamination using graphene and ZnO coupled photocatalysts: a review, Mater. Sci. Energy Technol. 2 (2019) 509–525, https://doi.org/10.1016/j.mset.2019.04.007.
[2] C.B. Ong, L.Y. Ng, A.W. Mohammad, A review of ZnO nanoparticles as solar photocatalysts: synthesis, mechanisms and applications, Renew. Sustain. Energy Rev. 81 (2018) 536–551, https://doi.org/10.1016/j.rser.2017.08.020.
[3] R. Mahdavi, S.S.A. Talesh, Sol-gel synthesis, structural and enhanced photocatalytic performance of Al doped ZnO nanoparticles, Adv. Powder Technol. 28 (2017) 1418–1425, https://doi.org/10.1016/j.apt.2017.03.014.
[4] H. Lu, S. Wang, L. Zhao, J. Li, B. Dong, Z. Xu, Hierarchical ZnO microarchitectures assembled by ultrathin nanosheets: hydrothermal synthesis and enhanced photocatalytic activity, J. Mater. Chem. 21 (2011) 4228–4234, https://doi.org/10.1039/c0jm03390a.
[5] A. Jiamprasertboon, S.C. Dixon, S. Sathasivam, M.J. Powell, Y. Lu, T. Siritanon, C. J. Carmalt, Low-cost one-step fabrication of highly conductive ZnO:Cl transparent thin films with tunable photocatalytic properties via aerosol-assisted chemical vapor deposition, ACS Appl. Electron. Mater. 1 (2019) 1408–1417, https://doi.org/10.1021/acsaelm.9b00190.
[6] R. Georgekutty, M.K. Seery, S.C. Pillai, A highly efficient Ag-ZnO photocatalyst: synthesis, properties, and mechanism, J. Phys. Chem. C. 112 (2008) 13563–13570, https://doi.org/10.1021/jp802729a.
[7] C. Tian, Q. Zhang, A. Wu, M. Jiang, B. Jiang, H. Fu, Cost-effective large-scale synthesis of ZnO photocatalyst with excellent performance for dye photodegradation, Chem. Commun. 48 (2012) 2858–2860, https://doi.org/10.1039/c2cc16434e.
[8] Y. Zong, Z. Li, X. Wang, J. Ma, Y. Men, Synthesis and high photocatalytic activity of Eu-doped ZnO nanoparticles, Ceram. Int. 40 (2014) 10375–10382, https://doi.org/10.1016/j.ceramint.2014.02.123.
[9] B. Subash, B. Krishnakumar, R. Velmurugan, M. Swaminathan, M. Shanthi, Synthesis of Ce co-doped Ag-ZnO photocatalyst with excellent performance for NBB dye degradation under natural sunlight illumination, Catal. Sci. Technol. 2 (2012) 2319–2326, https://doi.org/10.1039/c2cy20254a.
[10] M. Ahmad, E. Ahmed, Y. Zhang, N.R. Khalid, J. Xu, M. Ullah, Z. Hong, Preparation of highly efficient Al-doped ZnO photocatalyst by combustion synthesis, Curr. Appl. Phys. 13 (2013) 697–704, https://doi.org/10.1016/j.cap.2012.11.008.
[11] A.B. Patil, K.R. Patil, S.K. Pardeshi, Enhancement of oxygen vacancies and solar photocatalytic activity of zinc oxide by incorporation of nonmetal, J. Solid State Chem. 184 (2011) 3273–3279, https://doi.org/10.1016/j.jssc.2011.10.016.
[12] V. Kumari, A. Mittal, J. Jindal, S. Yadav, N. Kumar, S-, N- and C-doped ZnO as semiconductor photocatalysts: a review, Front. Mater. Sci. 13 (2019) 1–22, https://doi.org/10.1007/s11706-019-0453-4.
[13] L. Shi, L. Liang, J. Ma, Y. Meng, S. Zhong, F. Wang, J. Sun, Highly efficient visible light-driven Ag/AgBr/ZnO composite photocatalyst for degrading Rhodamine B, Ceram. Int. 40 (2014) 3495–3502, https://doi.org/10.1016/j.ceramint.2013.09.080.
[14] H. Ma, L. Yue, C. Yu, X. Dong, X. Zhang, M. Xue, X. Zhang, Y. Fu, Synthesis, characterization and photocatalytic activity of Cu-doped Zn/ZnO photocatalyst with carbon modification, J. Mater. Chem. 22 (2012) 23780–23788, https://doi.org/10.1039/c2jm35110b.
[15] W. Liu, M. Wang, C. Xu, S. Chen, Facile synthesis of g-C3N4/ZnO composite with enhanced visible light photooxidation and photoreduction properties, Chem. Eng. J. 209 (2012) 386–393, https://doi.org/10.1016/j.cej.2012.08.033.
[16] G. Yang, Z. Yan, T. Xiao, Preparation and characterization of SnO 2 /ZnO/TiO 2 composite semiconductor with enhanced photocatalytic activity, Appl. Surf. Sci. 258 (2012) 8704–8712, https://doi.org/10.1016/j.apsusc.2012.05.078.
[17] Z.R. Tian, J.A. Voigt, J. Liu, B. Mckenzie, M.J. Mcdermott, M.A. Rodriguez, H. Konishi, H. Xu, Complex and oriented ZnO nanostructures, Nat. Mater. 2 (2003) 821–826, https://doi.org/10.1038/nmat1014.
[18] J.L. Zhao, X.M. Li, S. Zhang, C. Yang, X.D. Gao, W.D. Yu, Highly (002)-oriented ZnO film grown by ultrasonic spray pyrolysis on ZnO-seeded Si (100) substrate, J. Mater. Res. 21 (2006) 2185–2190, https://doi.org/10.1557/jmr.2006.0291.
[19] Y. Lin, H. Hu, Y.H. Hu, Role of ZnO morphology in its reduction and photocatalysis, Appl. Surf. Sci. 502 (2020), 144202, https://doi.org/10.1016/j.apsusc.2019.144202.
[20] D. Vernardou, G. Kenanakis, S. Couris, E. Koudoumas, E. Kymakis, N. Katsarakis, pH effect on the morphology of ZnO nanostructures grown with aqueous chemical growth, Thin Solid Films 515 (2007) 8764–8767, https://doi.org/10.1016/j.tsf.2007.03.108.
[21] J. Yan, G. Wu, N. Guan, L. Li, Z. Li, X. Cao, Understanding the effect of surface/bulk defects on the photocatalytic activity of TiO2: Anatase versus rutile, Phys. Chem. Chem. Phys. 15 (2013) 10978–10988, https://doi.org/10.1039/c3cp50927c.
[22] L. Lang, D. Wu, Z. Xu, Controllable fabrication of TiO2 1D-nano/micro structures: Solid, hollow, and tube-in-tube fibers by electrospinning and the photocatalytic performance, Chem. A Eur. J. 18 (2012) 10661–10668, https://doi.org/10.1002/chem.201200378.
[23] M. Maeng, S. Choi, N.K. Shahi, S. Dockko, Experimental approaches for identifying the impact of enhanced flotation technology using hollow microspheres, J. Environ. Manag. 253 (2020), 109690, https://doi.org/10.1016/j.jenvman.2019.109690.
[24] O. Friedl, C. Motz, H. Peterlik, S. Puchegger, N. Reger, R. Pippan, Experimental investigation of mechanical properties of metallic hollow sphere structures, Metall. Mater. Trans. B Process. Metall. Mater. Process. Sci. 39 (2008) 135–146, https://doi.org/10.1007/s11663-007-9098-2.
[25] L. Zhou, H. Xu, H. Zhang, J. Yang, S.B. Hartono, K. Qian, J. Zou, C. Yu, Cheap and scalable synthesis of α-Fe2O3 multi-shelled hollow spheres as high-performance anode materials for lithium ion batteries, Chem. Commun. 49 (2013) 8695–8697, https://doi.org/10.1039/c3cc43867h.
[26] N. Parveen, Z. Khan, S.A. Ansari, S. Park, S.T. Senthilkumar, Y. Kim, H. Ko, M. H. Cho, Feasibility of using hollow double walled Mn2O3 nanocubes for hybrid Na-air battery, Chem. Eng. J. 360 (2019) 415–422, https://doi.org/10.1016/j.cej.2018.11.228.
[27] L. Zhou, Z. Zhuang, H. Zhao, M. Lin, D. Zhao, L. Mai, Intricate hollow structures: controlled synthesis and applications in energy storage and conversion, Adv. Mater. 29 (2017), 1602914, https://doi.org/10.1002/adma.201602914.
[28] T. Gyulavári, K. Kovács, Z. Kovács, E. Bárdos, G. Kovács, K. Baán, K. Magyari, G. Veréb, Z. Pap, K. Hernadi, Preparation and characterization of noble metal modified titanium dioxide hollow spheres – new insights concerning the light trapping efficiency, Appl. Surf. Sci. 534 (2020), 147327, https://doi.org/10.1016/j.apsusc.2020.147327.
[29] H.A. Borbón-Nuñez, D. Dominguez, F. Muñoz-Muñoz, J. Lopez, J. Romo-Herrera, G. Soto, H. Tiznado, Fabrication of hollow TiO2 nanotubes through atomic layer deposition and MWCNT templates, Powder Technol. 308 (2017) 249–257, https://doi.org/10.1016/j.powtec.2016.12.001.
[30] Z. Lou, Y. Wang, Y. Yang, Y. Wang, C. Qin, R. Liang, X. Chen, Z. Ye, L. Zhu, Carbon sphere template derived hollow nanostructure for photocatalysis and gas sensing, Nanomaterials 10 (2020) 19–21, https://doi.org/10.3390/nano10020378.
[31] X. Wang, P. Hu, Y. Fangli, L. Yu, Preparation and characterization of ZnO hollow spheres and ZnO−carbon composite materials using colloidal carbon spheres as templates, J. Phys. Chem. C. 111 (2007) 6706–6712, https://doi.org/10.1021/jp070382w.
[32] C. Jin, K. Zhu, G. Peterson, Z. Jian, G. Xu, Y. Wei, C. Ge, J. Li, Morphology dependent photocatalytic properties of ZnO nanostructures prepared by a carbon-sphere template method, J. Nanosci. Nanotechnol. 18 (2018) 5234–5241, https://doi.org/10.1166/jnn.2018.15471.
[33] P. Song, Q. Wang, Z. Yang, Acetone sensing characteristics of ZnO hollow spheres prepared by one-pot hydrothermal reaction, Mater. Lett. 86 (2012) 168–170, https://doi.org/10.1016/j.matlet.2012.07.058.
[34] K. Qi, B. Cheng, J. Yu, W. Ho, Review on the improvement of the photocatalytic and antibacterial activities of ZnO, J. Alloy. Compd. 727 (2017) 792–820, https://doi.org/10.1016/j.jallcom.2017.08.142.
[35] R. Kavitha, S.G. Kumar, A review on plasmonic Au-ZnO heterojunction photocatalysts: preparation, modifications and related charge carrier dynamics, Mater. Sci. Semicond. Process. 93 (2019) 59–91, https://doi.org/10.1016/j.mssp.2018.12.026.
[36] Y. Zhang, Q. Wang, J. Xu, S. Ma, Synthesis of Pd/ZnO nanocomposites with high photocatalytic performance by a solvothermal method, Appl. Surf. Sci. 258 (2012) 10104–10109, https://doi.org/10.1016/j.apsusc.2012.06.083.
[37] T.S. Tofa, F. Ye, K.L. Kunjali, J. Dutta, Enhanced visible light photodegradation of microplastic fragments with plasmonic platinum/zinc oxide nanorod photocatalysts, Catalysts 9 (2019) 819, https://doi.org/10.3390/catal9100819.
[38] Y. Wang, C. Yan, L. Chen, Y. Zhang, J. Yang, Controllable charge transfer in Ag-TiO2 composite structure for SERS application, Nanomaterials 7 (2017) 1–11, https://doi.org/10.3390/nano7070159.

[39] X. Li, W. Feng, Y. Xiao, P. Sun, X. Hu, K. Shimanoe, G. Lu, N. Yamazoe, Hollow zinc oxide microspheres functionalized by Au nanoparticles for gas sensors, RSC Adv. 4 (2014) 28005–28010, https://doi.org/10.1039/c4ra02541e.
[40] G. Kovács, S. Fodor, A. Vulpoi, K. Schrantz, A. Dombi, K. Hernádi, V. Danciu, Z. Pap, L. Baia, Polyhedral Pt vs. spherical Pt nanoparticles on commercial titanias: Is shape tailoring a guarantee of achieving high activity? J. Catal. 325 (2015) 156–167, https://doi.org/10.1016/j.jcat.2015.02.008.
[41] Á. Kmetykó, K. Mogyorósi, P. Pusztai, T. Radu, Z. Kónya, A. Dombi, K. Hernádi, Photocatalytic H2 evolution using different commercial TiO2 catalysts deposited with finely size-tailored au nanoparticles: critical dependence on Au particle size, Materials 7 (2014) 7615–7633.
[42] C. Singhal, C.S. Pundir, J. Narang, A genosensor for detection of consensus DNA sequence of Dengue virus using ZnO/Pt-Pd nanocomposites, Biosens. Bioelectron. 97 (2017) 75–82, https://doi.org/10.1016/j.bios.2017.05.047.
[43] Z.B. Yu, Y.P. Xie, G. Liu, G.Q. (Max) Lu, X.L. Ma, H.-M. Cheng, Self-assembled CdS/Au/ZnO heterostructure induced by surface polar charges for efficient photocatalytic hydrogen evolution, J. Mater. Chem. A. 1 (2013) 2773–2776, https://doi.org/10.1039/C3TA01476B.
[44] A.K. Zak, W.H.A. Majid, M.E. Abrishami, R. Youse, X-ray analysis of ZnO nanoparticles by Williamson – Hall and size – strain plot methods X-ray analysis of ZnO nanoparticles by Williamson e Hall and size e strain plot methods, Solid State Sci. 13 (2013) 251–256, https://doi.org/10.1016/j.solidstatesciences.2010.11.024.
[45] T.M. Project, Materials Data on ZnO by Materials Project, (2020). https://doi.org/10.17188/1196748.
[46] Y. Wang, W. Tang, L. Zhang, Crystalline size effects on texture coefficient, electrical and optical properties of sputter-deposited Ga-doped ZnO thin films, J. Mater. Sci. Technol. 31 (2015) 175–181, https://doi.org/10.1016/j.jmst.2014.11.009.
[47] B. Réti, G.I. Kiss, T. Gyulavári, K. Baan, K. Magyari, K. Hernadi, Carbon sphere templates for TiO2 hollow structures: preparation, characterization and photocatalytic activity, Catal. Today 284 (2017) 160–168, https://doi.org/10.1016/j.cattod.2016.11.038.
[48] S.M. Mousavi, A.R. Mahjoub, R. Abazari, Green synthesis of ZnO hollow sphere nanostructures by a facile route at room temperature with efficient photocatalytic dye degradation properties, RSC Adv. 5 (2015) 107378–107388, https://doi.org/10.1039/c5ra19507a.
[49] S. Krishnamurthy, A. Esterle, N.C. Sharma, S.V. Sahi, Yucca-derived synthesis of gold nanomaterial and their catalytic potential, Nanoscale Res. Lett. 9 (2014) 1–9, https://doi.org/10.1186/1556-276X-9-627.
[50] M. Zhang, B. Zhou, K.T. Chuang, Catalytic deep oxidation of volatile organic compounds over fluorinated carbon supported platinum catalysts at low temperatures, Appl. Catal. B Environ. 13 (1997) 123–130, https://doi.org/10.1016/S0926-3373(96)00097-5.
[51] Z. Kovács, C. Molnár, U.L. Štangar, V.M. Cristea, Z. Pap, K. Hernadi, L. Baia, Optimization Method of the Solvothermal Parameters Using Box–Behnken Experimental Design—The Case Study of ZnO Structural and Catalytic Tailoring, Nanomaterials 11 (2021) 1334, https://doi.org/10.3390/nano11051334.
[52] S. Tachikawa, A. Noguchi, T. Tsuge, M. Hara, O. Odawara, H. Wada, Optical properties of zno nanoparticles capped with polymers, Materials 4 (2011) 1132–1143, https://doi.org/10.3390/ma4061132.
[53] Y. Lv, C. Pan, X. Ma, R. Zong, X. Bai, Y. Zhu, Production of visible activity and UV performance enhancement of ZnO photocatalyst via vacuum deoxidation, Appl. Catal. B Environ. 138–139 (2013) 26–32, https://doi.org/10.1016/j.apcatb.2013.02.011.
[54] B. Choudhury, A. Choudhury, Oxygen defect dependent variation of band gap, Urbach energy and luminescence property of anatase, anatase-rutile mixed phase and of rutile phases of TiO2 nanoparticles, Phys. E Low. Dimens. Syst. Nanostruct. 56 (2014) 364–371, https://doi.org/10.1016/j.physe.2013.10.014.
[55] P. Norouzzadeh, K. Mabhouti, M.M. Golzan, R. Naderali, Investigation of structural, morphological and optical characteristics of Mn substituted Al-doped ZnO NPs: a Urbach energy and Kramers-Kronig study, Opt. (Stuttg.) 204 (2020), 164227, https://doi.org/10.1016/j.ijleo.2020.164227.
[56] A. Prakash, D. Bahadur, Chemically derived defects in zinc oxide nanocrystals and their enhanced photo-electrocatalytic activities, Phys. Chem. Chem. Phys. 16 (2014) 21429–21437, https://doi.org/10.1039/c4cp03583f.
[57] A.B. Djurisic, Y. Leung, K. Tam, L. Ding, W. Ge, H.-Y. Chen, S. Gwo, Green, yellow, and orange defect emission from ZnO nanostructures: Influence of excitation wavelength, Appl. Phys. Lett. 88 (2006), 103107, https://doi.org/10.1063/1.2182096.
[58] A. Galdámez-Martinez, G. Santana, F. Güell, P.R. Martínez-Alanis, A. Dutt, Photoluminescence of zno nanowires: a review, Nanomaterials 10 (2020) 857, https://doi.org/10.3390/nano10050857.
[59] P. Fageria, S. Gangopadhyay, S. Pande, Synthesis of ZnO/Au and ZnO/Ag nanoparticles and their photocatalytic application using UV and visible light, RSC Adv. 4 (2014) 24962–24972, https://doi.org/10.1039/C4RA03158J.
[60] H.Y. Lin, C.L. Cheng, Y.Y. Chou, L.L. Huang, Y.F. Chen, K.T. Tsen, Enhancement of band gap emission stimulated by defect loss, Opt. Express 14 (2006) 2372–2379, https://doi.org/10.1364/OE.14.002372.
[61] J. Yuan, E.S.G. Choo, X. Tang, Y. Sheng, J. Ding, J. Xue, Synthesis of ZnO-Pt nanoflowers and their photocatalytic applications, Nanotechnology 21 (2010), 185606, https://doi.org/10.1088/0957-4484/21/18/185606.
[62] J.M. Lin, H.Y. Lin, C.L. Cheng, Y.F. Chen, Giant enhancement of bandgap emission of ZnO nanorods by platinum nanoparticles, Nanotechnology 17 (2006) 4391–4394, https://doi.org/10.1088/0957-4484/17/17/017.
[63] A. Chugh, S. Ramachandran, A. Tiwari, J. Narayan, Epitaxial ZnO/Pt layered structures and ZnO-Pt nanodot composites on sapphire (0001), J. Electron. Mater. 35 (2006) 840–845, https://doi.org/10.1007/BF02692537.
[64] M. Zare, K. Namratha, S. Alghamdi, Y.H.E. Mohammad, A. Hezam, M. Zare, Q. A. Drmosh, K. Byrappa, B.N. Chandrashekar, S. Ramakrishna, X. Zhang, Novel green biomimetic approach for synthesis of ZnO-Ag nanocomposite; antimicrobial activity against food-borne pathogen, biocompatibility and solar photocatalysis, Sci. Rep. 9 (2019) 1–15, https://doi.org/10.1038/s41598-019-44309-w.
[65] M. aouicha Bouayed, N. Ameur, F. Taieb-Brahimi, T. Hidouri, S. Naser, H. Ghouas, S. Bedrane, B.M. Al-Shahri, R. Bachir, Investigation of novel titanate nanotubes modified with Ce, Fe, Zn and Zr for efficient dye degradation performance, inhibition of bacterial and fungal growth and anticorrosion activity in acid medium, React. Kinet. Mech. Catal. 134 (2021) 517–537, https://doi.org/10.1007/s11144-021-02068-8.
[66] M. Machovsky, I. Kuritka, J. Sedlak, M. Pastorek, Hexagonal ZnO porous plates prepared from microwave synthesized layered zinc hydroxide sulphate via thermal decomposition, Mater. Res. Bull. 48 (2013) 4002–4007, https://doi.org/10.1016/j.materresbull.2013.06.018.
[67] Y. Wang, Y. Li, Z. Zhou, X. Zu, Y. Deng, Evolution of the zinc compound nanostructures in zinc acetate single-source solution, J. Nanopart. Res. 13 (2011) 5193–5202, https://doi.org/10.1007/s11051-011-0504-y.
[68] S. Meephon, T. Rungrotmongkol, S. Puttamat, S. Praserthdam, V. Pavarajarn, Heterogeneous photocatalytic degradation of diuron on zinc oxide: influence of surface-dependent adsorption on kinetics, degradation pathway, and toxicity of intermediates, J. Environ. Sci. 84 (2019) 97–111, https://doi.org/10.1016/j.jes.2019.04.016.
[69] C. Feng, Z. Chen, J. Jing, J. Hou, The photocatalytic phenol degradation mechanism of Ag-modified ZnO nanorods, J. Mater. Chem. C 8 (2020) 3000–3009, https://doi.org/10.1039/c9tc05010h.
[70] S. Malato, J. Cáceres, A.R. Fernández-Alba, L. Piedra, M.D. Hernando, A. Agüera, J. Vial, Photocatalytic treatment of diuron by solar photocatalysis: evaluation of main intermediates and toxicity, Environ. Sci. Technol. 37 (2003) 2516–2524, https://doi.org/10.1021/es0261170.
[71] K.D. Ngwashi, B.M.R. Cross, S. Paul, P.M. Andrian, A. Devi, High Mobility ZnO thin film transistors using the novel deposition of high-k dielectrics, MRS Online Proceedings Library 1315 (2011) 618, https://doi.org/10.1557/opl.2011.721.
[72] A. Ismail, M.J. Abdullah, The structural and optical properties of ZnO thin films prepared at different RF sputtering power, J. King Saud. Univ. Sci. 25 (2013) 209–215, https://doi.org/10.1016/j.jksus.2012.12.004.
[73] F. Chowdhury, Influence of thickness variation on the optical properties of ZnO thin films prepared by thermal evaporation method, J. Electron Devices 10 (2011) 448–455.